Supporting Information

Jung et al. 10.1073/pnas.1206121109

SI Text

SI Methods. ***Role of substrate on droplet freezing.*** Water droplet freezing was investigated on PMMA, titanium, and copper surfaces. The salient nature of the temperature variations in supercooled sessile droplets (using thermocouple T1, see Fig. 4) are shown in Fig. S1, which only plots the measurements on PMMA and copper substrates as a function of time during the entire freezing process.

From this figure, the different freezing stages can be clearly recognized. The first recalescent stage is too fast (lasts 20 ms± 3 ms) to be captured in detail by the time resolution of the thermocouple and appears as the first temperature jump in Fig. S1 *A* and *B*. During this stage of freezing, only a fraction of the liquid volume freezes into an ice scaffold while the latent heat of freezing is almost entirely absorbed by the resulting ice-water mixture. The absorption of the released latent heat mainly by the ice-water mixture is evident in the similarity of the time needed for the first stage (recalescent) freezing and the measured droplet temperature at the end of it (see Fig. S1 *A* and *B*), regardless of the substrate thermal conductivity. Therefore, at the end of the first stage a simple heat balance (1) results in $m_I/m_W = [c_W/(\Delta h_m - c_I)]\Delta T \approx 0.22$, where m and c denote the mass and specific heat capacity; subscripts I and W respectively represent the ice and the liquid water; and Δh_m and ΔT respectively denote the specific latent heat of melting and the degree of supercooling. The second stage, lasting for 41 s ± 5 s and 3.1 s ± 0.4 s on PMMA and copper, respectively, can also be clearly identified in Fig. S1. The freezing time on titanium was measured to be 8.8 s ± 1.5 s. On PMMA, after the first stage, the resulting ice-water slush reached 0 °C. The temperature of the slush remained at 0 °C on PMMA for the second freezing stage. Since the tip of T1 was fixed (at approximately 0.7 mm from the substrate surface), the isothermal character of stage two on PMMA was only visible until the freezing front passed by the thermocouple at time $t = \sim$20 s (Fig. S1*A*). This isothermal phase was absent on copper (Fig. S1*B*). In addition, the freezing front of the second stage on copper propagated considerably faster upwards, away from the substrate [see experimentally observed front positions (solid triangles) in Fig. S2].

It is expected that the high thermal conductivity of copper would provide a low-resistance path for dissipation of the heat released during freezing. Overall, the shown temperature variation can be understood to result from a balance of the heat produced at the freezing front with heat conducted in to the substrate, and heat dissipation to the environment through a combination of evaporation and convection.

The accurate modeling of the freezing process is very involved, in part due to the need to capture the moving interface behavior, requiring a dedicated specialized investigation. Previous works have used numerical approaches to study the freezing of sessile droplets (2). However, to understand the basic behavior of the role of the substrate thermal conductivity, a goal pursued in the present study, one can simply consider a one-dimensional Stefan-type freezing problem (3) with a realistic determination of the liquid substrate temperature. During the rapid recalescent stage, the temperature of the droplet rises very rapidly; thus, we can safely assume the substrate temperature to remain temporarily unaffected. Therefore, postrecalescence, we obtain the temperature of the substrate using an analytical expression for the interface temperature developing when two semiinfinite regions are brought to contact (4)

$$T_i = \frac{\sqrt{(k\rho c_p)_{\text{sub}}}T_{\text{sub}} + \sqrt{(k\rho c_p)_{\text{drop}}}T_{\text{drop}}}{\sqrt{(k\rho c_p)_{\text{sub}}} + \sqrt{(k\rho c_p)_{\text{drop}}}}, \qquad \textbf{[S1]}$$

where the subscripts sub and drop represent the substrate and droplet, respectively. The variables k, ρ, c_p denote the thermal conductivity, the density and the heat capacity, respectively (1, 5). With a substrate temperature of −14.5 °C, a droplet freezing temperature of 0 °C, and substituting the property values for copper, titanium, and PMMA, the interface temperatures were determined to be −13.9 °C, −11.4 °C, and −3.3 °C, respectively. Clearly the poor conductivity of PMMA offers high resistance for heat conduction, thereby resulting in higher interface temperature.

The interface temperature in Eq. **S1** can be used as a boundary condition in a simplified, one-dimensional Stefan-type freezing problem with the liquid temperature held at 0 °C to relate the location of the freezing front with time t as (3)

$$s(t) = 2\lambda(\alpha_I t)^{1/2}, \qquad \textbf{[S2]}$$

where $\alpha_I = k_I/\rho_I c_{p,I}$ denotes the thermal diffusivity of ice and λ is a constant to be determined from a transcendental energy balance equation at interface given by (3):

$$\lambda e^{\lambda^2}\text{erf}(\lambda) = \frac{c_{p,I}(T_I - T_{\text{drop}})}{\Delta H_m\sqrt{\pi}}, \qquad \textbf{[S3]}$$

where ΔH_m denotes the enthalpy of fusion (1). Eq. **S3** was solved to determine λ for different substrates. Fig. S2 compares the analytically predicted (Eq. **S2** and blue curves in Fig. S2) and experimentally observed (black triangles in Fig. S2) evolution of the freezing front positions for the two extreme cases, copper and PMMA. The matching slopes of the experimental and theoretical trends for the evolution of the freezing interface location testify to the validity of the power law variation expressed in Eq. **S2**.

The experimental data were obtained by analysis of the digitized images obtained from the video recording the droplet freezing in side view (see for example s_1–s_3 in Fig. S3, indicating the instantaneous position of the freezing front on PMMA). The experimentally observed evolution of the freezing front position was $s(t) = 0.1748t^{1/2}$ for PMMA (red dashed curve in Fig. S2*A*) and $s(t) = 0.6352t^{1/2}$ for copper (red dashed curve in Fig. S2*B*). This shows that our simple, one-dimensional estimate predicts the scaling of front propagation with time very well and differs only in constant prefactor from the experimentally observed front propagation dynamics.

Accounting for the amount of liquid water already frozen in the first stage (S2) (approximately 22%; see estimation above), the remaining freezing time t_2 on copper, titanium, and PMMA was calculated to be 5.8 s, 7.1 s, and 24.8 s, respectively. Clearly, the analytical results, while differing in actual values from the measured ones, confirm in a relative sense the decisive role of thermal conductivity on the freezing of the sessile droplet.

Critical supersaturation needed for condensation. According to the classic nucleation theory (6, 7), the critical supersaturation in vapor concentration needed for water condensation on a planar substrate depends strongly on surface wettability (contact angle). Supersaturation for water nucleation on solid surfaces as a function of water contact angle was first computed by Fletcher (8) using parameters determined from rain cloud experiments.

Although strictly valid only for ideally smooth surfaces, the analysis helps to provide a preliminary understanding of the salient thermodynamic properties involved in the water vapor condensation process and is outlined here in brief.

The rate of surface nucleation of condensed water from water vapor can be expressed as (6)

$$J = K\exp(-\frac{\Delta G_c}{k_B T}), \qquad \textbf{[S4]}$$

where k_B, T denote the Boltzmann constant and the temperature, respectively. The pre-factor K in Eq. **S4** designates a kinetic coefficient (6), which was estimated by Fletcher (7) to be of the order of 10^{24} to 10^{27} $cm^{-2}\,s^{-1}$.

The free energy of heterogeneous nucleation of water on a planar substrate is given by (1)

$$\Delta G_c = \frac{16\pi M^2 \gamma_{W,v}^3}{3(RT\rho_W \ln S)^2} f = \frac{A}{(\ln S)^2} f, \qquad \textbf{[S5]}$$

with the surface wetting factor (9)

$$f(\theta) = (2+\cos\theta)(1-\cos\theta)^2/4, \qquad \textbf{[S6]}$$

where M, $\gamma_{W,v}$, R, ρ_W, θ, and S respectively denote the molecular weight of water, the interfacial energy liquid water–water vapor (1), the universal gas constant, the liquid water density (1), the water droplet contact angle on the substrate, and the degree of critical saturation for water vapor condensation. Substituting Eq. **S5** into Eq. **S4** and rearranging the variables led to the desired expression of the critical saturation for water vapor nucleation as

$$S(\theta) = \exp\left(1/\sqrt{-\frac{\ln(J/K)}{Af(\theta)}}\right). \qquad \textbf{[S7]}$$

Assuming a nucleation rate of $J = 1$ $cm^{-2}\,s^{-1}$ (7) and considering an averaged water contact angle $\theta = 72°$, the critical saturation for water vapor (Eq. **S7**) is solved to be $S = 2.38$, which corresponds to a critical supersaturation value of 138%. This critical supersaturation value differs from the slightly above the 100% value at which condensation is recorded in the experiments (see main text). Mahata et al. (8) studied the effect of water contact angle on the condensation process and confirmed a significant deviation in the critical supersaturation values predicted theoretically and observed experimentally with increasing contact angle. For example, for PMMA surface with an average water contact angle of approximately 80° the deviation was approximately 130%, which lies within the expected range compared to the present findings.

However, in *Influence of humidity and substrate thermal conductivity on evaporation and condensation during freezing* we discuss an alternative approach for determining the critical supersaturation on PMMA by modeling an ablimating ice crystal. The determined value of 104% ± 4% for critical saturation on PMMA with this approach is in accordance with our experiments.

Evaluation of water condensation/evaporation. Movie S1 shows the freezing and related water vapor evaporation and condensation around a sessile droplet on a PMMA surface. This section analyzes the phase change process in detail. Fig. S4 shows the radial width of condensate formed during freezing of sessile droplets on PMMA ($d_1 = 1.4$ mm, Fig. S4 *A* and *C*—Δt_1) and copper ($d_1 = 0.54$ mm, Fig. S4 *B* and *D*—Δt_1). Due to the approximately 14 times faster freezing on copper than on PMMA and the much faster temperature and water saturation reduction near the droplet–gas interface with time (initial slope of −16 °C/s on copper compared to a constant temperature of −0.5 °C for the first 20 s on PMMA, compare Fig. S1 *A* and *B*), the amount of evaporated, diffused, and condensed water is considerably lower on copper. Given that the vapor diffusion timescale for our conditions is $\tau_D \sim 0.1$ s and the initial slope of temperature reduction on copper is −1.6 °C/s, it can be clearly seen that the quasisteady approximation used for PMMA in the main document will fail on copper. Therefore, for very conductive substrates such as copper, a complex transient conjugate energy transport model, along with interface capturing at the freezing front and at the droplet evaporation surface, needs to be employed in order to predict the condensate formation and its spreading. The timescale of water vapor diffusion ensures a lesser amount of water condensation (as evident by lesser maximum width of the condensate d_1 in Fig. S4) on copper than on PMMA.

Due to the lesser amount of condensation in the vicinity of the freezing droplet on copper compared to PMMA, the condensate evaporates completely before freezing. The resulting vapor can have two different outcomes. It can mix with the ambient gas and/or deposit on to the frozen water droplet through ablimation [direct vapor–solid phase transition, (1, 10)]. The latter outcome is possible because the vapor pressure over a supercooled water surface is larger than that over an ice surface, resulting in a supersaturation state with respect to ice and in a vapor flux from the liquid to the frozen droplet. The supersaturation over ice can be expressed as $S_I = (p_{sat,W}/p_{sat,I}) - 1 = 0.145$, where $p_{sat,W}$, $p_{sat,I}$ respectively denote the saturation vapor pressure over plane water and ice surfaces at −14.5 °C (1). The vapor flux to ice results in growth of an ice crystal at the expense of neighboring liquid microdroplets by the Wegener–Bergeron–Findeisen mechanism (1).

This is clearly visible through formation of an inner edge in the condensate near droplet contact line (inner dashed line in Fig. S4*D*), which recedes from the droplet contact line with time due to evaporation of the condensate. We should note here that this is in spite of the fact that during the evaporation stage more water condenses near the mother droplet contact line than away from it (i.e., the maximum size of the condensate drops near the contact line is higher than of those away from it). The change in position of this inner edge with time is plotted as blue circles in Fig. S4*B*. Eventually, the inner and outer edges merge together (overlap of red square and blue circle at 2.3 s in Fig. S4*D*), indicating the absence of any condensation remnant in the neighborhood of the mother droplet.

Also visible in the magnified segment of Fig. S4*C*—Δt_2 is the absence of liquid microdrops in the vicinity of the frozen condensate edge (gap between frozen and liquid condensate), because of their evaporation onto the growing crystals (Wegener–Bergeron–Findeisen mechanism, as described above). *Diffusion controlled ice crystal growth* discusses this phenomenon in more detail.

Influence of humidity and substrate thermal conductivity on evaporation and condensation during freezing. Fig. S5 illustrates that the ambient humidity and substrate thermal conductivity of the substrate directly control the amount of condensed water and thus its maximum expanse. With a rise in humidity the water vapor concentration necessary to reach supersaturation reduces, resulting in an increase in the maximum expanse of condensed water. The opposite outcome is observed with an increase in the substrate thermal conductivity, which results in an increase in the rate at which the latent heat released due to freezing is transmitted through the substrate, and therefore leads to a faster freezing of the droplet volume (see also *Role of substrate on droplet freezing* and *Evaluation of water condensation/evaporation* for more details).

Diffusion controlled ice crystal growth. As outlined in the main text, in the performed experiments there was a time gap of 8.3 s

between complete freezing of one droplet (including its condensate) and the initiation of freezing of the neighboring droplet. The time difference between completion of freezing of one droplet and initiation of the neighboring one is also clear from the freezing of droplet arrays recorded in Movie S2. It was discussed in that context that a water-free zone is formed between the outer edge of the frozen condensate and the neighboring liquid droplet contact line (see Fig. 3). In this zone (bounded on one side by the white dashed lines in Fig. 3) the vapor concentration remains below critical supersaturation concentration so as to avoid water condensation on the sample surface. A similar, albeit much smaller, gap is also observed in front of the freezing condensate from an isolated droplet in Fig. S4*C*—Δt_2 (zoomed image), where a water-free zone is formed between the edges of frozen and liquid condensate. The reason for formation of both these gaps is ablimation due to different saturated vapor concentrations between ice and water as discussed above. However, the gap between the freezing condensate edge and the remaining condensate microdroplets is very small, which should facilitate continuous advancement in the freezing condensate edge. This explains the continuous freezing of the condensate in Movie S1. On the other hand, the gap in Fig. 3*B* between the condensate edge and the second liquid droplet (approximately 14 μm) is large. Below, we analyze the experimentally determined time an ice crystal needs to overcome this gap zone (Fig. 3*B*) and use the outcome to re-evaluate the critical humidity for water condensation on PMMA compared to the approach discussed in *Critical supersaturation needed for condensation*.

The vapor mass flux at the ice crystal surface for a temperature of −14.5 °C can be expressed as (1)

$$\frac{dm}{dt} \approx \frac{C}{G} S_I, \qquad \textbf{[S8]}$$

with

$$G = \frac{\frac{RT}{p_{\mathrm{sat},I} D_v M} + \frac{\Delta H_s}{k_g T}\left(\frac{\Delta H_s M}{RT} - 1\right)}{4\pi} = 3.8 \times 10^6 \ \mathrm{m\,s\,kg^{-1}}, \qquad \textbf{[S9]}$$

where ΔH_s, D_v, $p_{\mathrm{sat},I}$, and S_I denote the specific heat of sublimation, the diffusivity of water vapor, the water vapor saturation pressure, and the degree of supersaturation with respect to ice at −14.5 °C, respectively (1). The parameter $C = 2a_0/\pi$, with a_0 denoting the initial radius of a geometrically idealized circular ice crystal (1). Assuming the shape of the growing ice crystal to be a simple thin, circular ice disc with radius a and height δ, the mass flux in Eq. **S8** can be written as

$$a\frac{da}{dt} \approx \frac{1}{\rho_I \pi \delta}\frac{C}{G} S_I = \Gamma, \qquad \textbf{[S10]}$$

where ρ_I denotes the density of ice [919 kg/m^3 at −14.5 °C (1)].

Integration of Eq. **S10** results in

$$a(t) \approx \sqrt{2\Gamma t + a_0^2}. \qquad \textbf{[S11]}$$

Fig. S6 displays the theoretical change in the crystal size (a–a_0) with time for a model ablimating ice particle (Eq. **S11**). The time at which the crystal size increases to overcome the gap size (approximately 14 μm) must be the time at which we observe the initiation of the freezing of the neighboring droplet. Two different water vapor concentrations are used: saturated condition (which corresponds to $S_I = 14.5\%$; blue curve in Fig. S6) and approximately 8% supersaturated condition (which corresponds to $S_I = 24\%$; red curve in Fig. S6) at −14.5 °C. The initial radius and height of the growing ice particle used were 2.75 μm and 2.11 μm, estimated from the size of a frozen condensed microdroplet close to the water- and ice-free gap (see Fig. 3*B*).

Also shown in Fig. S6 is the experimentally determined time (8.3 s) an incipient growing ice crystal needs in order to overcome the water- and ice-free gap of approximately 14 μm before initiating nucleation at the neighboring liquid droplet (cross in Fig. S6; compare also with the Fig. 3 *B*, *C*, and *D*).

It is important to realize that the vapor concentration at the outermost edge of the condensate in Fig. 3*B* must be equal to the critical supersaturation needed for condensation. In fact, that is what determines the expanse of condensate. The concentration is likely to remain the same over the frozen microdroplets in the condensate. Therefore, the vapor concentration in the gap between the frozen condensate and the second neighboring droplet will vary from critical supersaturation at the frozen condensate to saturation condition (with respect to water). The growth of ice crystals, assuming the vapor concentration to be saturated with respect to water ($S_I = 14.5\%$; blue curve in Fig. S6), underestimates the experimentally observed time of 8.3 s (cross in Fig. S6). On the other hand, for an assumed supersaturation of approximately 8% ($S_I = 24\%$; red curve in Fig. S6), the model overestimates the experiment. Therefore, the average humidity ϕ in the gap can be estimated to be $104 \pm 4\%$. The concentration could also be seen as the critical saturation needed for water condensation on PMMA. Improving the classical nucleation theory (*Critical supersaturation needed for condensation*), the above discussion confirms the findings presented in Fig. 2 of a critical saturation condition close to 100%.

Numerical model for quasisteady vapor diffusion. As discussed in the main document, the evaporation from a supercooled droplet freezing on an insulating substrate such as PMMA can be modeled using a quasisteady approach, with the approximation that vapor field adjustment due to vapor diffusion in ambient occurs much more rapidly than the rate of freezing front movement. The approach is justified because, as estimated in the main text, for a droplet freezing on PMMA, the freezing time τ_f of approximately 41 s is considerably larger than vapor diffusion time τ_D of approximately 0.1 s. In the following, the evaporation of the droplet during the second, thermally controlled stage of freezing is modeled, since the formation of condensation halo took place during this stage. The temperature of the slush (consisting of an ice crystal scaffold and water) freezing completely during this stage is assumed to remain at 0 °C. Please see Fig. S1*A* and the corresponding discussion in *Role of substrate on droplet freezing*.

Under quasistatic approximation, the vapor field around the droplet can be obtained by solving the steady vapor diffusion equation for the vapor mass concentration $\nabla^2 \rho_v = 0$. The upward motion of the freezing front continuously reduces the volume of the not-completely frozen region above it, and correspondingly continuously reduces the unfrozen surface area of the droplet through which the evaporation takes place. In spite of this complexity, further plausible simplifications in the modeling geometry can still be made as follows. With the assumption of spherical cap geometry for the droplet and the experimental observation that the freezing front remains parallel to the substrate surface as it moves upwards (Fig. S3), the vapor diffusion can be considered axisymmetric. For the quasisteady process modeled here, the time dependent movement of the freezing front and, therefore, the change in the available surface area of evaporation, can be obtained by processing the digitized images from the side view video recording of the droplet freezing process. More details on the experimental freezing front motion so obtained are described in *Role of substrate on droplet freezing*.

For every time step and corresponding area of evaporation, the vapor diffusion was modeled with axisymmetric, steady Laplace diffusion equation using the commercial software COMSOL®, ver. 4.2. Since only the second stage of freezing is modeled, to

account for the fact that 22% of the liquid is already transformed into ice after recalescence (see the estimate in *Role of substrate on droplet freezing*), the vapor concentration at the droplet surface was taken to be 0.78 ρ_{s0} where ρ_{s0} is the saturation vapor concentration at 0 °C. This is justified if the temperature of the slush (ice-water mixture) resulting from recalescence is 0 °C. In effect, this amounts to considering the second freezing stage to be similar to a Stefan-type freezing problem, where the liquid temperature is held at the interface equilibrium temperature (11). The temperature measurement inside the droplet once the freezing front passes the thermocouple tip justifies this assumption.

The concentration at far field is derived from the relative humidity of 1.3% measured at the experimental chamber temperature of −14.5 °C. The far field boundary was taken at $160R_0$, where R_0 is the initial contact line radius of the sessile droplet. As the freezing interface moves upward, the surface area of evaporation is reduced. The already frozen bottom part of the droplet does not contribute to evaporation. This is implemented by setting the gradients in the vapor concentration equal to zero in the frozen part of the droplet surface. The gradient is also set to zero at the substrate.

Fig. S7 shows the contour plots for the vapor field concentrations at two specific positions of the freezing front. An unstructured triangular mesh was used for the simulation. In order to capture the high-concentration gradients occurring near the droplet-air interface, the grids were kept 100 times finer near the interface compared to the low gradient, far field region. The maximum grid size was kept at 2 mm and the maximum allowed rate of increase in the grid size was kept at 10%. These grid sizes were obtained through a systematic grid independence study for an intermediate position of the freezing interface. A relative tolerance of 1×10^{-6} was used as convergence criterion for all simulations.

Fig. S7 shows the vapor contours at two instants at which tangents to the droplet at the point of intersection of the freezing front with the droplet air interface are at 60° (Fig. S7*A*) and 36° (Fig. S7*B*) from the horizontal freezing front. In essence, we can think of this as akin to evaporation from a droplet with variable contact angle. However, the key difference lies in the fact that as the freezing front starts to move, the remaining slush rests on the formed ice. Clearly this angle is equal to 73° initially—i.e., equal to the equilibrium contact angle on the substrate—and falls to 0° at the end of the freezing process. The entire second freezing stage was modeled through parametric variation of the geometry using 2° steps in the contact angle on ice. This amounted to separate steady-state simulations for each contact angle, at steps differing by 2°, which was justified due to the quasisteady nature of the evaporation process. The parametric sweep feature in the COMSOL® solver was used to obtain the solutions. Volume expansion upon freezing of about 9% is neglected in this approximate calculation because the corresponding change in area will be even smaller. Therefore, the assumption should not appreciably affect the evaporation process.

1. Pruppacher H, Klett JD (1998) *Microphysics of Clouds and Precipitation* (Kluwer, Dordrecht, Boston, London).
2. Tabakova S, Feuillebois F (2004) On the solidification of a supercooled liquid droplet lying on a surface. *J Coll Int Sci* 272:225–234.
3. Özisik MN (1993) *Heat Conduction* (Wiley Interscience, New York), pp 392–435.
4. Cengel YA (2007) *Heat and Mass Transfer: A Practical Approach* (McGraw-Hill, New York), pp 276.
5. Lide DR, ed (2007) *Handbook of Chemistry and Physics* (CRC, Boca Raton, FL).
6. Fletcher NH (1958) Size effect in heterogeneous nucleation. *J Chem Phys* 29: 572–576.
7. Fletcher NH (1962) *Physics of Rain Clouds* (Cambridge Univ Press, Cambridge, UK).
8. Mahata PC (1975) Insoluble condensation nuclei: the effect of contact angle, surface roughness and adsorption. *J Atmos Sci* 32:116–121.
9. Turnbull D, Fisher JC (1949) Rate of nucleation in condensed systems. *J Chem Phys* 17:71–73.
10. Hoke JL, Georgiadis JG, Jacobi AM (2004) Effect of substrate wettability on frost properties. *J Thermophys Heat Trans* 18:228–235.
11. Jiji LM (2009) *Heat Conduction* (Springer, Berlin, Heidelberg).

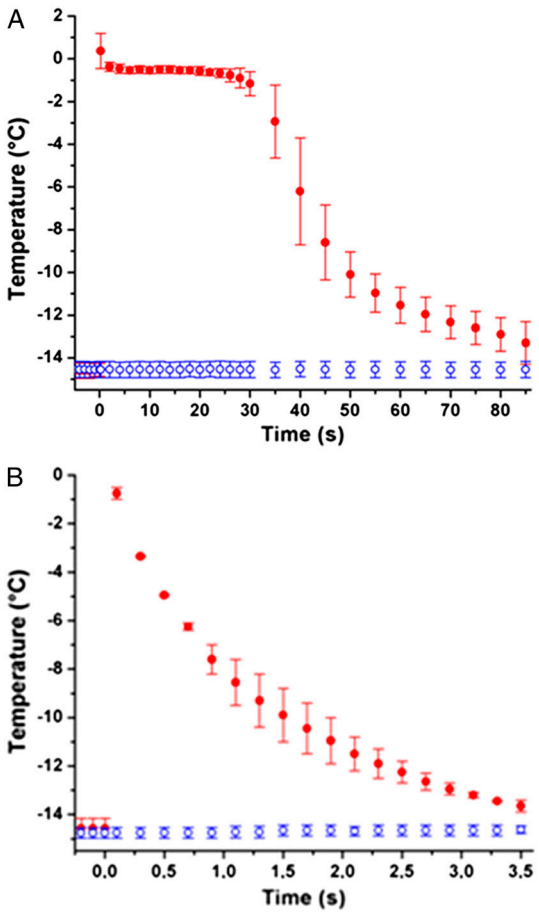

Fig. S1. Variation of water droplet temperatures. Temperature variation with time for a freezing water droplet on PMMA (*A*) and copper (*B*) substrate. The temperatures were measured at 10 Hz; however, for clarity, a smaller time resolution appears in the figures. The red closed dots indicate the temperature in the droplet at approximately 0.7 mm from the substrate while the blue circles represent the gas temperature. The error bars indicate the standard deviation out of three measurements. The first red points before recalescence in (*A*) are not visible.

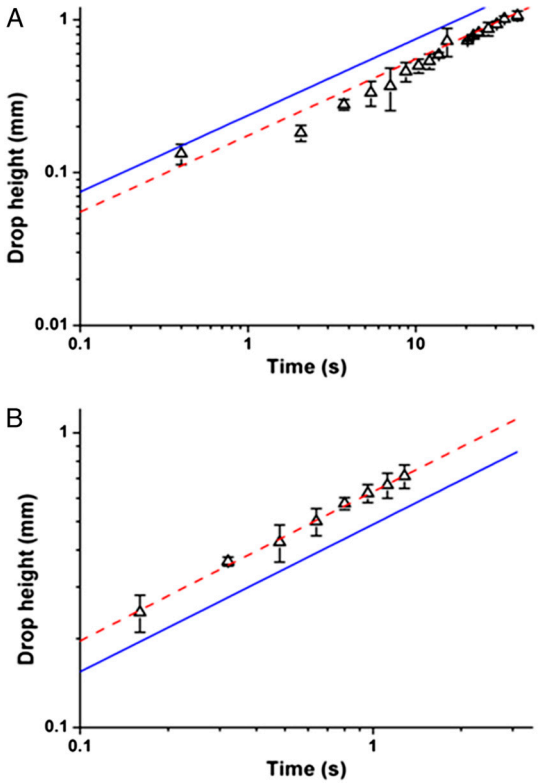

Fig. S2. Freezing front distribution. (*A*) Calculated (blue curve) and experimentally determined (solid triangles) freezing front moving upward and parallel to the PMMA substrate. (*B*) Calculated (blue curve) and experimentally determined (solid triangles) freezing front moving upward and parallel to the copper substrate. The fitting of the experimental data is indicated by the red dashed curves. The error bars indicate the standard deviation out of three measurements.

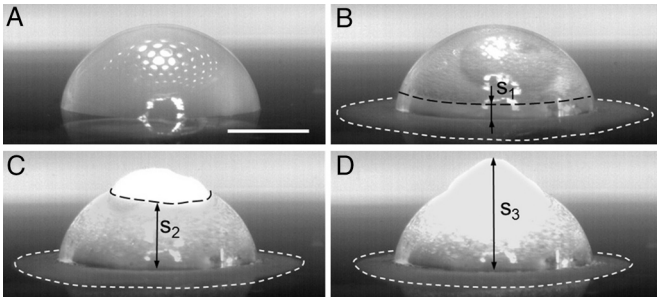

Fig. S3. Side view of a freezing water droplet on PMMA. (*A*–*D*) Showing snapshots at 0.3, 10, 30, and 45 s. (*A*) Freezing water droplet soon after the first freezing stage. (*B*–*C*) The second stage of droplet freezing. The freezing front moves upward and parallel to the substrate, indicated by the black dashed line. (*D*) Completely frozen water droplet. s_1–s_3 indicate the instantaneous positions of the freezing front. The white dashed lines indicate the outer boundary of condensed water. The scale bar equals 1 mm.

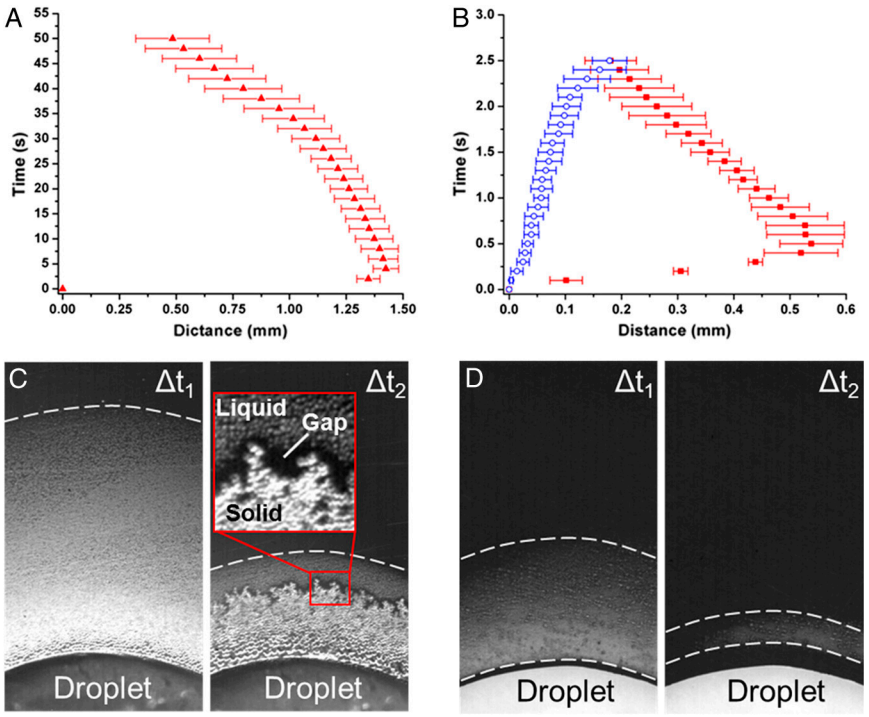

Fig. S4. Diffusion controlled water condensation and evaporation. (*A*) Variation in position of condensate outer edge with time on PMMA (red closed triangles). (*B*) Condensate halo outer (red closed squares) and inner (blue circles) edge position variation with time on copper. (*C*) Position of condensate outer edge (dashed line), maximum expanse (Δt_1), and during condensate evaporation (Δt_2) on PMMA. (*D*) Position of condensate outer and inner edge (dashed lines), maximum expanse (Δt_1), and during condensate evaporation (Δt_2) on copper. Note the absence of condensate in the vicinity of frozen condensed water [magnified segment in (*C*) Δt_2] and the frozen mother droplet (*D*) due its evaporation into the environment and ablimation onto the frozen water. The error bars represent the standard deviation over three measurements.

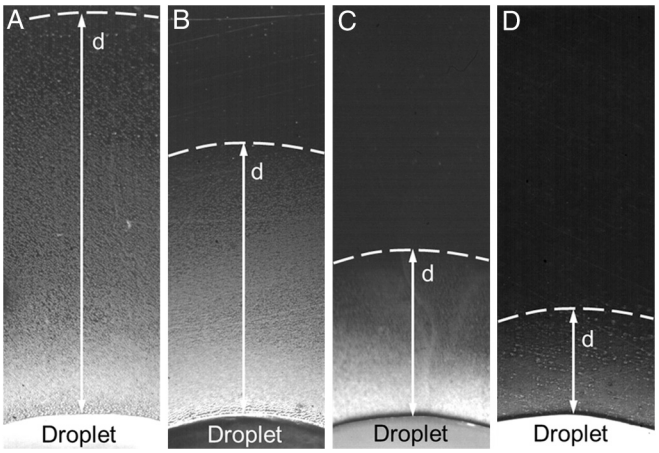

Fig. S5. Humidity and thermal conductivity controlled evaporation and condensation from a 5-μl freezing sessile water droplet. (*A*) Position of condensate outer edge on PMMA at 35% humidity (maximum expanse $d = \sim 2.2$ mm). (*B*) Position of condensate outer edge on PMMA and 1.3% humidity (maximum expanse $d = \sim 1.4$ mm). (*C*) Position of condensate outer edge on titanium and 1.3% humidity (maximum expanse $d = \sim 0.9$ mm). (*D*) Position of condensate outer edge on copper and 1.3% humidity (maximum expanse $d = \sim 0.55$ mm).

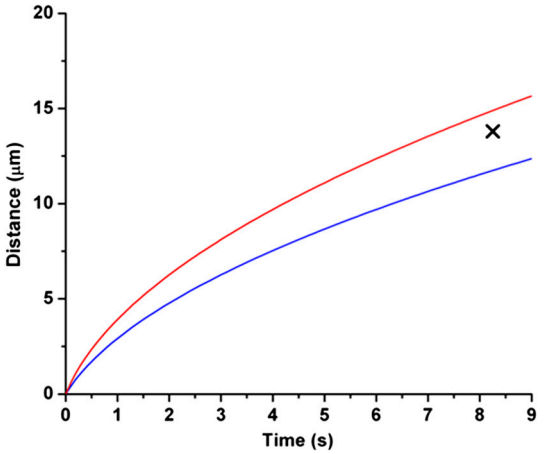

Fig. S6. Ablimating ice particle. Theoretical ice crystal growth through the water- and ice-free gap under different supersaturation values S_I with respect to ice ($S_I = 14.5\%$, blue curve and $S_I = 24\%$, red curve). The black cross represents the time an ice crystal needs to overcome the gap distance of approximately 14 μm observed in the experiment.

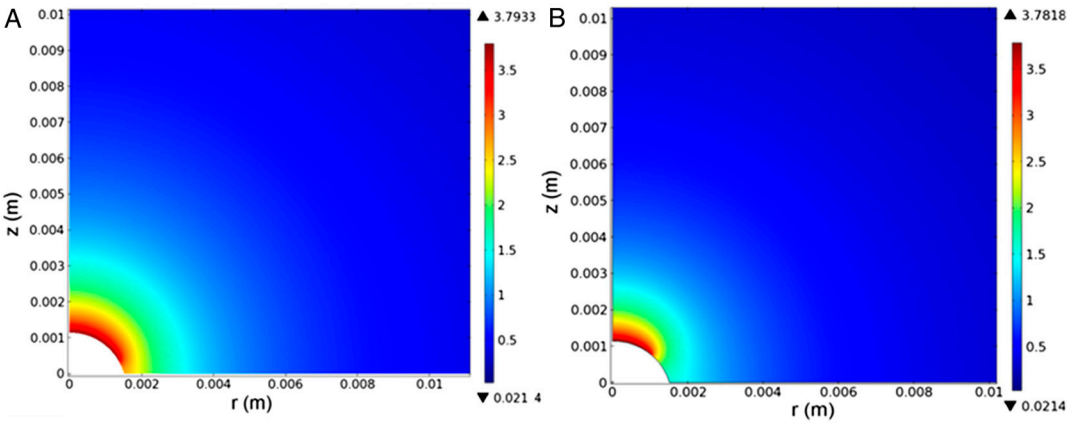

Fig. S7. Evaporation of freezing droplet. Vapor concentration field around a supercooled sessile droplet freezing on an insulating substrate and undergoing evaporation due to heat release during freezing. The unit of concentration is g/m^3. The vapor diffusion is quasisteady with respect to the freezing dynamics. (*A*) and (*B*) show two specific instants during the second stage of freezing.

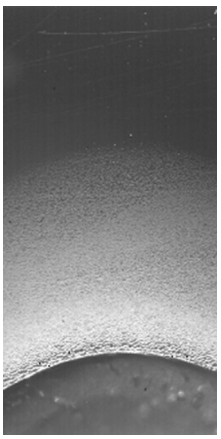

Movie S1. Diffusion controlled water condensation and evaporation during stage two of freezing. Initially, the droplet (magnified segment) is in a supercooled liquid state and in thermal equilibrium with the substrate and the gas at −14.5 °C. The bright ring concentric to the droplet contact line indicates the liquid and finally partial frozen condensate on the substrate. The microdroplets in the condensate should be closely spaced to each other. Therefore, the rapid freezing of the successive microdroplets in the condensate should be due to the fact that upon freezing every microdroplet must expand in volume and, thereby, contact its next neighboring microdrop. This process will initiate a chain-like freezing front propagation through the microdroplets in the condensate, which is exactly what we observe in the movie.

Movie S1 (MOV)

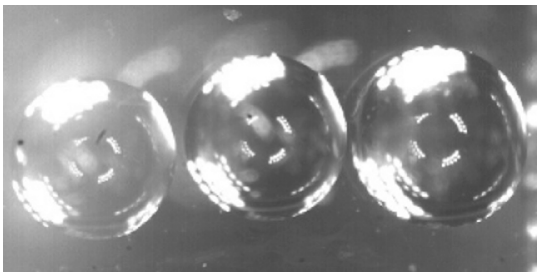

Movie S2. Evaporation, condensation and freezing of condensate on a droplet array. With evaporation and condensation formed from the freezing of an undercooled water droplet, frost condensate initiates ice nucleation in the neighboring droplet, resulting in a domino-like effect of independent water freezing. Initially, all three droplets are in thermal equilibrium with the PMMA substrate and the environment at −14.5 °C. The first crystallization of the right droplet is initiated in a controlled manner by bringing a small ice-cluster in contact with the liquid surface.

Movie S2 (MOV)